electronics

MDPI

Article

The Impact of Overlap Period on the Stability of Current-Controlled Alternate Arm Converter Based on *dq* Frame Impedance Analysis

Shan Jiang *, Felipe Arraño-Vargas, Zhiwei Shen and Georgios Konstantinou

School of Electrical Engineering and Telecommunications, UNSW Sydney, Sydney, NSW 2052, Australia; f.arranovargas@unsw.edu.au (F.A.-V.); zhiwei.shen@unsw.edu.au (Z.S.); g.konstantinou@unsw.edu.au (G.K.)
* Correspondence: shan.jiang4@unsw.edu.au

Abstract: As a variant modular converter configuration, the alternate arm converter (AAC) is well-suited for high-voltage power transmission and large-scale integration of renewables. In contrast to conventional multilevel converters, the director switches in the arms of AAC lead to the introduction of an overlap period, during which circuiting current can flow through the two arms in the same phase. Thus, fixed or variable overlap period control can be implemented in AAC systems so as to dynamically balance stored arm energy. However, the control of overlap period is linked to instability issues that might impede the safe operation of AAC systems, which are yet to be reported. In this paper, the stability of an AAC system is demonstrated based on measured grid and converter impedance, in conjunction with impedance-based stability criterion in the *dq* frame. The interaction between harmonic sources at AC and DC sides of the AAC system is analyzed to determine resonant frequencies in the AC current when any potential resonance is identified in the *dq* frame. Novel results with respect to the impact of overlap period on the system stability are obtained by depicting and comparing the Eigenloci in the polar plot, which are validated by real-time simulations.

Keywords: alternate arm converter; stability; *dq* frame; resonance; real-time digital simulation

Citation: Jiang, S.; Arraño-Vargas, F.; Shen, Z.; Konstantinou, G. The Impact of Overlap Period on the Stability of Current-Controlled Alternate Arm Converter Based on *dq* Frame Impedance Analysis. *Electronics* **2022**, *11*, 301. https://doi.org/10.3390/electronics11030301

Academic Editors: Juan Rodríguez Méndez and Aitor Vázquez Ardura

Received: 18 December 2021
Accepted: 17 January 2022
Published: 19 January 2022

1. Introduction

Nowadays, power converters are increasing in medium/high-voltage applications, e.g., HVDC power transmission and renewable energy integration [1]. As the common interface of renewables and distributed energy resources, converter systems often face issues of dynamic interactions with the power grid, especially in weak or remote grids [2–4]. The resonance caused by impedance interaction will affect the control performance of converter systems and amplify specific harmonics in the power system. Harmonics with fixed magnitude will affect the power quality and introduce extra power losses. In the worst-case scenario, constantly amplifying harmonics may trigger the relay protections deployed in the power system and lead to severe consequences, e.g., generator tripping, load shedding and even the outage of large-scale power networks [5].

There is growing research in the field of stability analysis techniques for converter systems. State-space modeling and impedance-based modeling are the most typical models used. State-space modeling analyzes the interaction between the converter and the grid based on the details of hardware setup and control designs of converters. This type of model gives deep insights into the relationship between unstable modes and specific state variables [6]. However, its practical application is limited as accurate device and control details are difficult to obtain. By contrast, impedance-based modeling treats the converter as a black box and demonstrates the system stability according to the Nyquist stability criterion based on its terminal impedance characteristics, which are obtainable from either data sheets that vendors are willing to openly share or direct measurements [7,8]. Impedance-based stability analysis can help to facilitate converter design tasks of practical engineers and to set specifications for converter integration required by system operators.

To date, the stability of common converters has been well predicted based on impedance-based analysis. The stability of two-level and modular multilevel converter has been analysed in [9,10], respectively. The root causes of converter-driven stability issues include grid-synchronization techniques [11], inappropriate control structures or untuned control parameters [5], and improper power filter design [12]. As a modular converter configuration used for high-voltage power transmission and large-scale renewable energy integration, the control aspects of alternate arm converter (AAC) have been discussed widely. The parameter selection method is proposed in [13] to achieve the desired voltage ripple of submodules. By utilizing the feature of overlap period, energy balancing control in [14] and zero-current switching control in [15] are proposed to optimize the performance of AAC systems, respectively. The interoperability of MMC and AAC in Hybrid HVDC Systems are explored in [16]. In [17], the phase-shift modulation is extended to the control frame of AAC systems so that the AAC system can be constructed in a cost-efficient way by substituting all full-bridge submodules with half-bridge submodules. However, the stability assessment of AAC systems has not been reported in current literature.

This paper firstly demonstrates the stability of an AAC converter according to the impedance-based stability criterion in the *dq* frame. The principle is explained based on the ratio of the measured grid and converter impedance matrix, also defined as the return ratio matrix. In order to accurately identify resonant frequencies, the impact of off-diagonal elements in *dq* impedance matrices, usually ignored, is considered. With the stability analysis technique, this paper reveals the impact of overlap period on the Eigenloci of return ratio matrix and the stability of the AAC system. The analysis is further supported by real-time simulation results using RSCAD and RTDS.

2. Equivalent Model of AAC and Impedance-Based Stability Criterion

2.1. Configuration and Equivalent Model of AAC

A common configuration of the AAC is illustrated in Figure 1a, with each phase of AAC converter including upper and lower arms. Each arm comprises a stack of H-bridge cells, a series of IGBT modules functioning as the director switch (DS) and one arm inductor (L_{arm}). In the normal operation, the upper and lower arms of the AAC system operate alternately under the control of the DSs, in order to generate the desired voltage waveform. The AAC system is integrated into the system via a Y/Δ transformer, and v_{pcc} and i_{pcc} denote the AC voltage and current measured at the point of common coupling (PCC). v_g is the voltage of the utility grid, with its equivalent inductance and resistance represented as L_g and R_g, respectively. More details regarding this model can be found in [18].

Figure 1b shows the equivalent model of the AAC system. As a grid-tied current controlled converter system, the AAC is represented using the Norton equivalent circuit [3]. The grid input impedance $Z_g(s)$ and converter output impedance $Z_{aac}(s)$, in Figure 1b, are critical to the stability of AAC systems, which can be measured by using the frequency scanning method. By injecting the harmonic current into the PCC, voltage and current perturbations at two sides of the PCC will reflect the impedances of both the converter and the grid. In this paper, the measurement is carried out by a RTDS component in the *dq* frame [10]. The *dq* frame helps to decouple the interaction of different frequency components in the grid, which facilitates the accurate recognition of resonant frequencies. Moreover, the wide application of *dq* decoupling control in the converter systems make it easier to analyze the interaction between the DC and AC side in the *dq* frame, something that will be discussed in detail in the following section.

In the *dq* frame, the grid input impedance $Z_g(s)$ and the converter output impedance $Z_{aac}(s)$ are both expressed as a 2×2 matrix. For the grid, $Z_g(s)$ is denoted as:

$$Z_g(s) = \begin{bmatrix} R_g + sL_g & -\omega_0 L_g \\ \omega_0 L_g & R_g + sL_g \end{bmatrix}, \quad (1)$$

where ω_0 is the fundamental angular frequency. To calculate the exact value of $Z_g(s)$, one needs to evaluate s as $j\omega^{dq}$ or $j(\omega^{abc} - \omega_0)$. Note that the fundamental frequency in abc frame corresponds to the DC component in the dq frame. The analytical solution of the grid impedance matrix allows us to evaluate the system stability under different values of grid strength, reflected by the short-circuit ratio (SCR) in this paper.

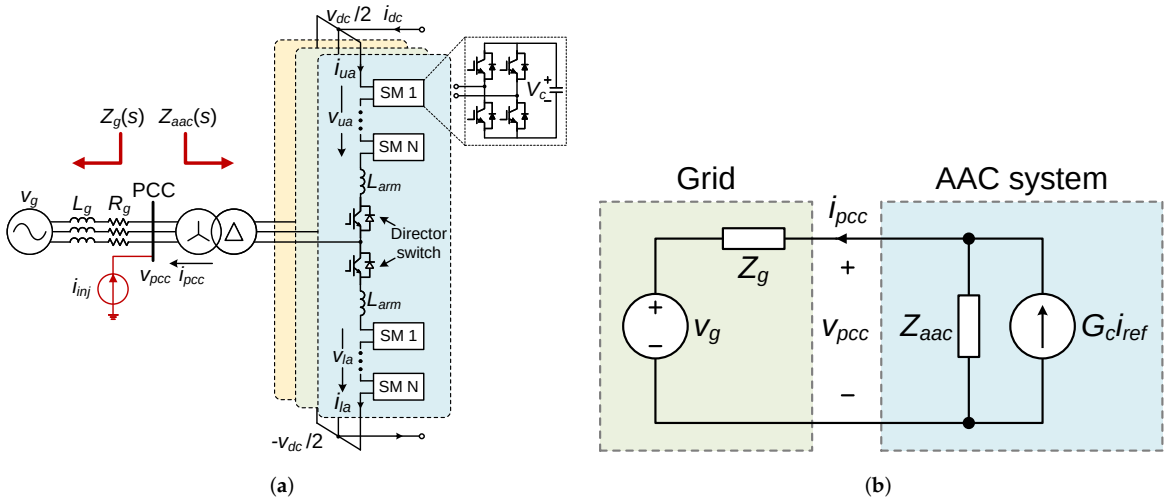

Figure 1. Configuration and equivalent model of a grid-tied current controlled AAC system: (**a**) basic structure; (**b**) equivalent model.

Compared with the grid impedance, the converter impedance is more complicated as it depends on the hardware circuit, control architecture and other aspects. Especially, the circulating current flows through two arms in the same phase during the overlap period and does not exist when the overlap period is over, which makes the control with respect to the overlap period a typical non-linear process. To simplify the analysis, the converter impedance $Z_{aac}(s)$ is measured using frequency scan method and is updated for any specific operating condition. For example, the profile of AAC impedance matrix when the overlap period is 20° is displayed in Figure 2.

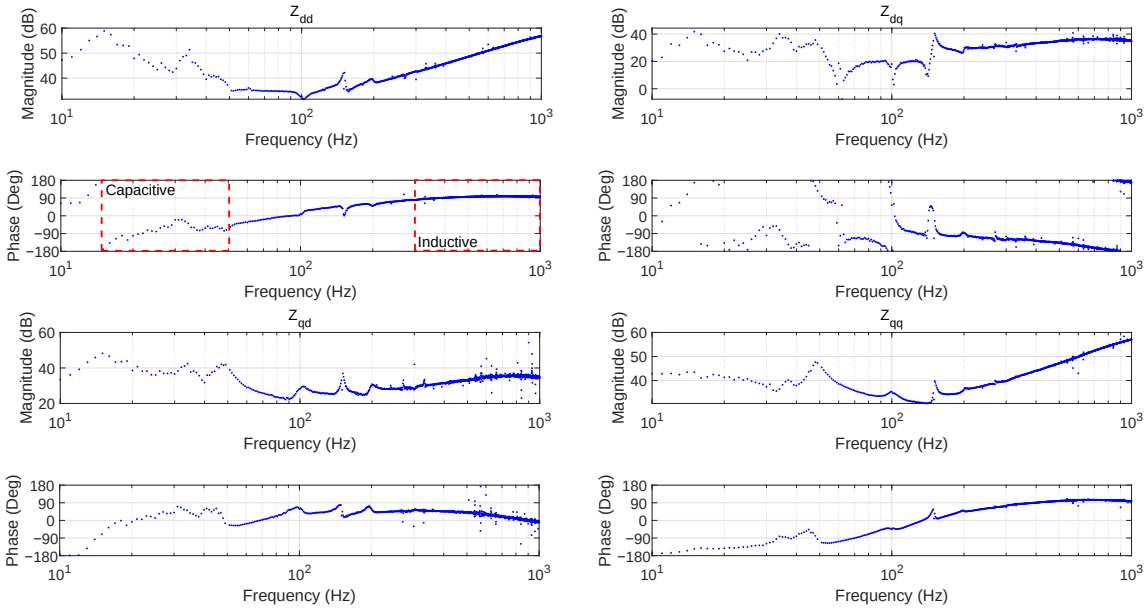

Figure 2. Frequency scan results of AAC converter impedance $Z_g(s)$ (overlap period is 20°).

According to the generalized Nyquist Criterion, the resonance issue caused by the dynamic interaction is easy to occur in a converter system when the phase difference between grid impedance Z_g and converter impedance Z_acc is close to 180°. As the grid impedance resembles an inductor at all frequency range, the AAC system is susceptible to resonance issues when its impedance resembles a capacitor, which is located at the low frequency range as shown in Figure 2. At the high frequency range, the AAC impedance is inductive due to its terminal transformer and arm inductors, which means the converter system is robust at this range.

2.2. Impedance-Based Stability Criterion in dq Frame

According to Figure 1b, the transfer function $i_{pcc}(s)/i_{ref}(s)$ is represented as:

$$\frac{i_{pcc}(s)}{i_{ref}(s)} = \frac{G_c(s)}{I + G(s)} = \frac{G_c(s)}{I + Z_g(s)Z_{aac}(s)^{-1}}, \tag{2}$$

where I represents a 2×2 identity matrix. The current gain $G_c(s)$ in (2) pertains to the closed-loop control frame of output current in the AAC system. For an AAC system, its closed-loop current controller is well designed to have enough phase margin at the crossover frequency, to guarantee internal stability. Therefore, this current gain $G_c(s)$ will not introduce right-half plane poles into the transfer function that might jeopardize system stability. That is to say, the stability of the grid-tied AAC system lies in the denominator of the expression in (2):

$$H(s) = I + G(s) = I + Z_g(s)Z_{aac}(s)^{-1}, \tag{3}$$

where $G(s) = Z_g(s)Z_{aac}(s)^{-1}$ is defined as the return ratio matrix. When $H(s)$ is not invertible, unexpected poles will be introduced into the transfer function and destablize the system. One effective way to demonstrate the stability is to analyze the Eigenvalues of $G(s)$ in (3). To illustrate the relationship between the Eigenvalues of $G(s)$ and the reversibility of $H(s)$, $G(s)$ can be decomposed in terms of Eigenvalues and Eigenvectors, as:

$$G(s) = Q\Lambda Q^{-1}, \tag{4}$$

where Q is the orthogonal 2×2 matrix whose i-th column is the unit Eigenvector of $G(s)$, and Λ is the diagonal matrix whose diagonal elements are two corresponding Eigenvalues, $\Lambda_{ii} = \lambda_i$. By introducing (4) into (3), (3) can be further expressed as:

$$H(s) = I + G(s) = QQ^{-1} + Q\Lambda Q^{-1} = Q(I + \Lambda)Q^{-1}. \tag{5}$$

Given that Q is an orthogonal matrix, i.e., $|Q| = |Q^{-1}| = 1$, the determinant of $H(s)$ is given as:

$$\det(H(s)) = |I + \Lambda| = (1 + \lambda_1)(1 + \lambda_2). \tag{6}$$

It reveals that $H(s)$ is not an invertible matrix and the system becomes unstable when any of the Eigenvalues of $G(s)$ equals or is close to -1, which can be identified in the Bode plot. In practical applications, a more conservative stability margin will be chosen based on either the gain margin (GM) or phase margin (PM) so that the system is stable to operate in a wider range. As shown in Figure 3, 6 dB GM and 30° PM will be adopted to demonstrate the system stability [9]. Any Eigenvalue of $G(s)$ that is located in the instability region encircled by the stability margin will be considered as a candidate for resonance at its corresponding frequency in the *dq* frame. From the physical point of view, the resonance tends to occur when control parameters/structures of the converter are not well designed or the converter is tied to a weak grid (or a strong grid but via a long transmission line).

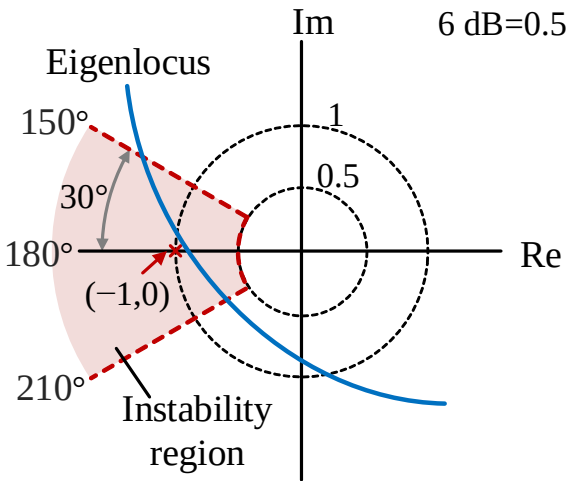

Figure 3. Instability region defined in the complex plane.

3. Stability Interaction between DC and AC Side of AAC Systems

Once a series of resonant frequencies are identified by the Eigenvalues of the return ratio matrix in the *dq* frame, the following step is to find the corresponding resonant frequencies in the AC current of the AAC system. In this section, the interaction between the DC and AC side of the AAC system and its impact on the AC resonant frequencies is discussed.

For the AAC system, the active power at the AC terminal is identical with the DC power:

$$P = \frac{3}{2}(v_{pcc}^{d} i_{pcc}^{d} + v_{pcc}^{q} i_{pcc}^{q}) = v_{dc} i_{dc}, \tag{7}$$

where $v_{pcc}^{d(q)}$ and $i_{pcc}^{d(q)}$ are d(q)-axis components of PCC voltage and current in the *dq* frame. v_{dc} and i_{dc} represent the voltage and current of DC bus in the AAC system, respectively. When resonance occurs in the system, harmonics will appear in both current and voltage waveforms. However, the AC voltage is sustained by the utility grid and the DC voltage is supported by dc-link capacitors, which keeps them relatively robust even in the event of resonance. Moreover, the phase locked loop (PLL) in the current controlled AAC system enables the PCC voltage to be d-axis oriented. With these conditions, the voltage components in (7) can be approximated as:

$$\begin{cases} v_{pcc}^{d} \approx V_{pcc} \\ v_{pcc}^{q} \approx 0 \\ v_{dc} \approx V_{dc} \end{cases}. \tag{8}$$

By contrast, DC and AC currents are more susceptible to the harmonics and distortions can be observed when the resonance occurs. Since the Eigenvalue analysis identifies resonant frequencies in the *dq* frame, the d-axis PCC current can be expressed as:

$$i_{pcc}^{d} = I_{pcc}^{d} + \hat{i}_{pcc}^{d} = I_{pcc}^{d} + \sum_{k=1}^{n} I_k sin(\omega_k^{dq} t + \phi_k), \tag{9}$$

where $\hat{i}_{pcc}^{d}$ represents a series of harmonics that contain n resonant frequencies. I_k and ϕ_k represent the magnitude and phase of harmonic current at the frequency of ω_k^{dq} that exists in the d-axis, respectively. By incorporating (8) and (9) into (7), it yields:

$$i_{dc} = I_{dc} + \hat{i}_{dc} = \frac{3V_{pcc}}{2V_{dc}} I_{pcc}^{d} + \frac{3V_{pcc}}{2V_{dc}} \sum_{k=1}^{n} I_k sin(\omega_k^{dq} t + \phi_k). \tag{10}$$

It shows that any harmonic current identified in the dq frame will excite the harmonic at the same frequency in the DC current. As the DC impedance is defined as the ratio of DC harmonic voltage to DC harmonic current, the harmonic voltage excited by corresponding harmonic current can be expressed with respect to the DC impedance:

$$\hat{v}_{dc} = \frac{3V_{pcc}}{2V_{dc}} \sum_{k=1}^{n} I_k |Z(j\omega_k^{dq})| sin(\omega_k^{dq} t + \phi_{zk}), \tag{11}$$

where $Z(j\omega_k^{dq})$ is the DC side impedance at ω_k^{dq} and $\phi_{zk} = \phi_k + \arg(Z(j\omega_k^{dq}))$. The harmonic sources at the DC side interact with the AC side under the function of the voltage modulation of AAC system [19]. The fundamental frequency component in the voltage modulation signal is considered to demonstrate the impact of harmonic sources at the DC side. Taking phase A as an example, the induced harmonic sources in the PCC voltage can be approximated as the product of insertion indices coming from the control frame and the DC bus voltage:

$$\begin{aligned} \hat{v}_{pcc} &\approx msin(\omega_0 t)\frac{\hat{v}_{dc}}{2} \\ &\approx \frac{3mV_{pcc}}{8V_{dc}} \sum_{k=1}^{n} I_k |Z(j\omega_k^{dq})| cos((\omega_0 - \omega_k^{dq})t - \phi_{zk}) \\ &- \frac{3mV_{pcc}}{8V_{dc}} \sum_{k=1}^{n} I_k |Z(j\omega_k^{dq})| cos((\omega_0 + \omega_k^{dq})t + \phi_{zk}), \end{aligned} \tag{12}$$

where m is the modulation index of the AAC system.

The harmonic voltage sources in (12) will finally excite harmonic currents at the AC terminal of the AAC system. Although the above discussion is established with some approximations, it reveals that each resonant frequency ω_k^{dq} identified in the dq frame will dominantly excite the harmonic with the same frequency in the DC current and a pair of resonant frequencies, i.e., $\omega_0 \pm \omega_k^{dq}$, in the AC current as shown in Figure 4.

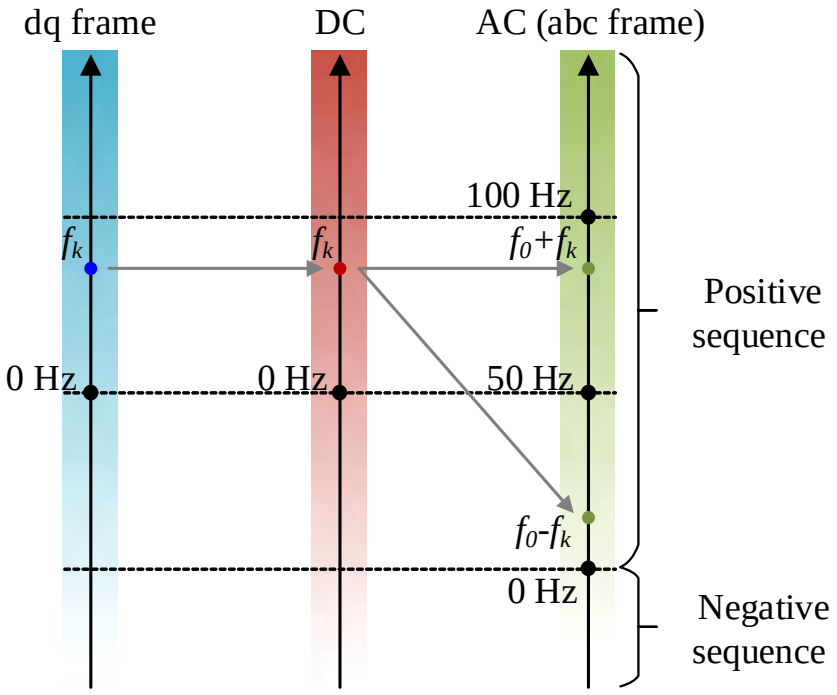

Figure 4. Propagation path of the resonant frequency in the AAC system.

4. Impact of Overlap Period on Stability of AAC Systems

The overlap period is a salient feature of AAC systems that makes them different from other converters. When the AC output voltage comes close to its zero-crossing point, DSs in both arms are switched on so that the circulating current flows through two arms to the DC side. This circulating current in the overlap period helps to balance the stored energy in the stacks and further balance all capacitor voltages of all SMs. Given the importance of overlap period to the operation of the AAC system, its impact on the system stability will be analyzed. For typical applications in reported literature [14,18,20,21], the overlap period (2α) ranges from 0° to 40°, which will be the main focus of the following discussion.

Figure 5 depicts two Eigenloci of the return ratio matrix $G(s)$, defined in (3), obtained from the AAC system with a SCR of 3.37. System parameters are given in Table 1. Note that the Eigenvalue locus of λ_2 is far from the instability region defined by the stability margin of GM 6 dB and PM 30°, which means it will have little impact on the system stability. Thus, only the dominant Eigenvalue λ_1 is considered in the stability analysis. For the dominant Eigenvalue λ_1, it is observed that the impact of overlap period dominantly lies in the low frequency range (10–150 Hz) in the dq frame and 150 Hz is the frequency of circulating component introduced by overlap period in the arm current. This range overlaps with the instability region in which the phase crosses $-180°$ and the magnitude is near 0 dB and brings in instability issues. When the frequency exceeds 150 Hz, the Eigenvalue locus with different overlap periods are almost the same and Eigenvalues of the return ratio matrix gradually moves away from the instability region.

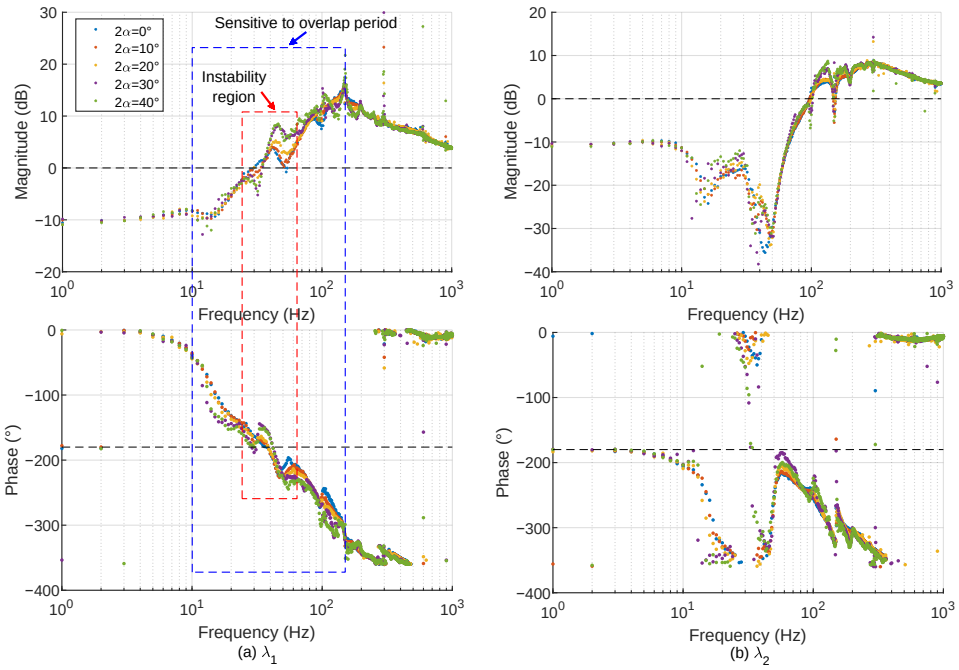

Figure 5. Bode plot of Eigenvalues of the return ratio matrix: (**a**) Eigenvalue λ_1; (**b**) Eigenvalue λ_2.

Table 1. System parameters.

Parameter	Value
PCC L-L voltage (RMS)	380 kV
DC voltage	400 kV
Reference active power	800 MW
Reference reactive power	0 MVar
Transformer ratio	380/280
L_g	0.17/0.065 H
R_g	4.5/2 Ω
SCR	3.37/8.80

To better illustrate the impact of overlap period, the polar plot of dominant Eigenvalue is shown in Figure 6. The impedance mismatching between the grid and the AAC leads the Eigenvalue locus into the instability region. With the overlap period increasing, the Eigenvalue locus has the tendency to engage more with the instability region. In other words, the increasing overlap period poses an increasing threat to the system stability. These Eigenvalues included in the instability region will be considered as candidates for the resonance and their corresponding frequencies become potential resonant frequencies. For the range of 1–100 Hz in the *dq* frame, any identified resonant frequency will correspond to one sub-synchronous resonant frequency and one super-synchronous resonant frequency in the abc frame.

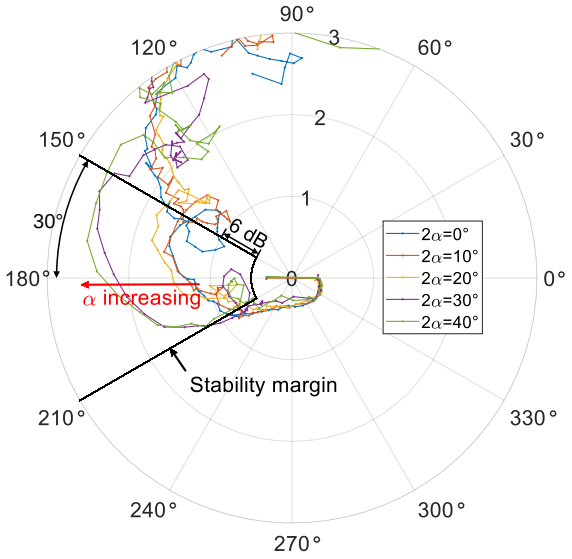

Figure 6. Polar plot of dominant Eigenvalue λ_1 of the return ratio matrix at low frequency range (1–100 Hz) in the *dq* frame.

5. Simulation Results and Discussions

The simulation model of the grid-tied current controlled AAC-HVDC system is established in RTDS, of which system parameters are shown in Table 1 [18]. The control frame of AAC systems includes high-level and low-level control parts. The high-level control adopts *PQ* controller to directly regulate the terminal power flow of the AAC system. The output of high-level control, AC reference voltages, will be given as the control input of low-level controllers, including SM sorting control, zero-current switching control, overlap period control, etc. As the main focus of this paper, the implementation of overlap period control is shown in Figure 7. The reference value of overlap period comes from either constant value or the energy balancing controller that regulates the stored arm energy. In this paper, the constant overlap period control is utilized to better evaluate the stability performance of AAC system with different overlap periods.

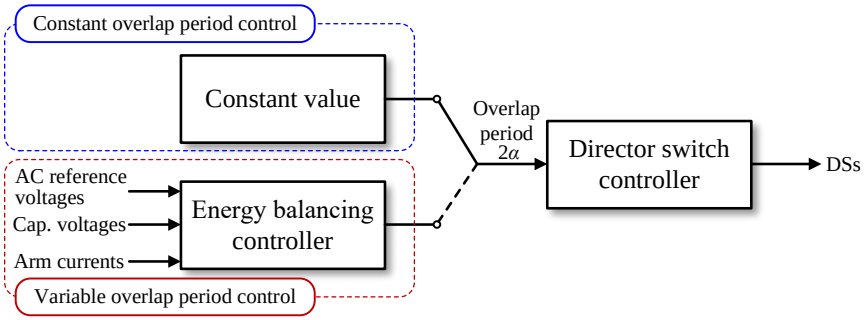

Figure 7. Implementation of overlap period control in an AAC system.

Four different values of the AAC overlap period, $2\alpha = 0, 10^\circ, 20^\circ$ and 40°, are considered to validate the impedance-based stability analysis in the dq frame and the impact of overlap period. The grid input impedance and converter output impedance are measured by the frequency scanning method using an RSCAD component [10]. The frequency scan is performed from 1 to 1000 Hz in the dq frame with a frequency resolution of 1 Hz. The classic synchronous reference frame (SRF)-PLL is adopted to synchronize the AAC system with the grid, and the bandwidth of SRF-PLL in the simulation model is set low enough so that its impact on the stability can be minimized.

Figure 8 depicts the polar plot of the dominant Eigenlocus of the return ratio matrix for all four cases, in which the SCR is set as 8.8. This relatively large SCR makes the AAC system with different overlap periods have different stability states. The Eigenloci of $2\alpha = 0^\circ$ and 10° are located at the edge of the instability region, which means the AAC system in these two cases is marginally stable. The Eigenloci of $2\alpha = 20^\circ$ and 40° engage more with the instability region and will consequently make the AAC system experience resonance. The potential resonant frequency for both cases ranges from 37 Hz to 45 Hz according to the Eigenvalues that are located in the instability region. However, as the Eigenvalue locus of $2\alpha = 40^\circ$ is much closer to the point $(-1, 0)$, the resonance will be more severe in this scenario.

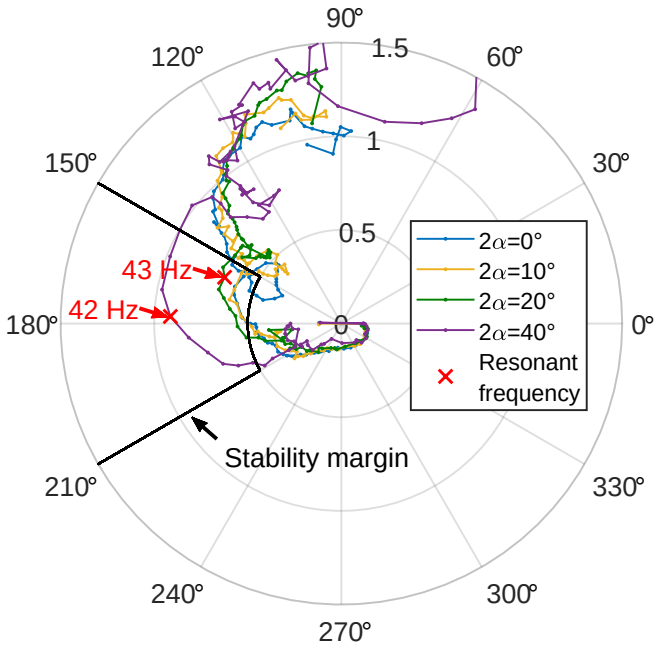

Figure 8. Polar plot of dominant Eigenvalue λ_1 of the return ratio matrix for different values of overlap period.

Simulation results of the AAC system for all four cases are given in Figure 9. It includes the waveforms of capacitor voltages in two arms of phase A, three-phase AC voltages and currents along with FFT results. For the first two cases, the AAC system is marginally stable and no obvious distortion is observed in the AC voltage, AC current as well as capacitor voltages. In Figure 9a,b, the total harmonic distortion (THD) of AC voltage and current is no more than 0.5%. In contrast, the AAC system is no longer stable when the overlap period is set as 20° and 40° as shown in Figure 9c,d. The ripples of capacitor voltages reach 40% and 75%, respectively. The AC current is obviously distorted and there is one pair of resonant peaks in the AC current that are recognizable for each case seeing from the FFT results. For the case of $2\alpha = 20^\circ$, the resonant frequencies in the abc frame are 7 Hz and 93 Hz, which correspond to 43 Hz frequency in the dq frame. For the case of $2\alpha = 40^\circ$, the resonant frequencies in the abc frame are 8 Hz and 92 Hz, which correspond to 42 Hz

in the *dq* frame. For both cases, the resonant frequencies in the *dq* frame are marked in Figure 8. These results coincide very well with the impedance-based stability analysis.

As the converter impedance is derived from the small-signal model, the stability analysis can be only carried out for any given steady state. To expand this method to dynamic operating conditions, the dynamic process can be divided into multiple steady states so that the stability of AAC system at each state can be evaluated separately. As shown in Figure 10, the dynamic process of parameter change occurs when $t = 0.2$ s, at which the overlap period changes from 40° to 0°. The AAC system is going through resonance issues with a large overlap period and the resonance components are well dampened with a smaller overlap period after the parameter change. It proves that stability analyses corresponding to steady states are also effective to predict the performance of AAC in dynamic operating conditions.

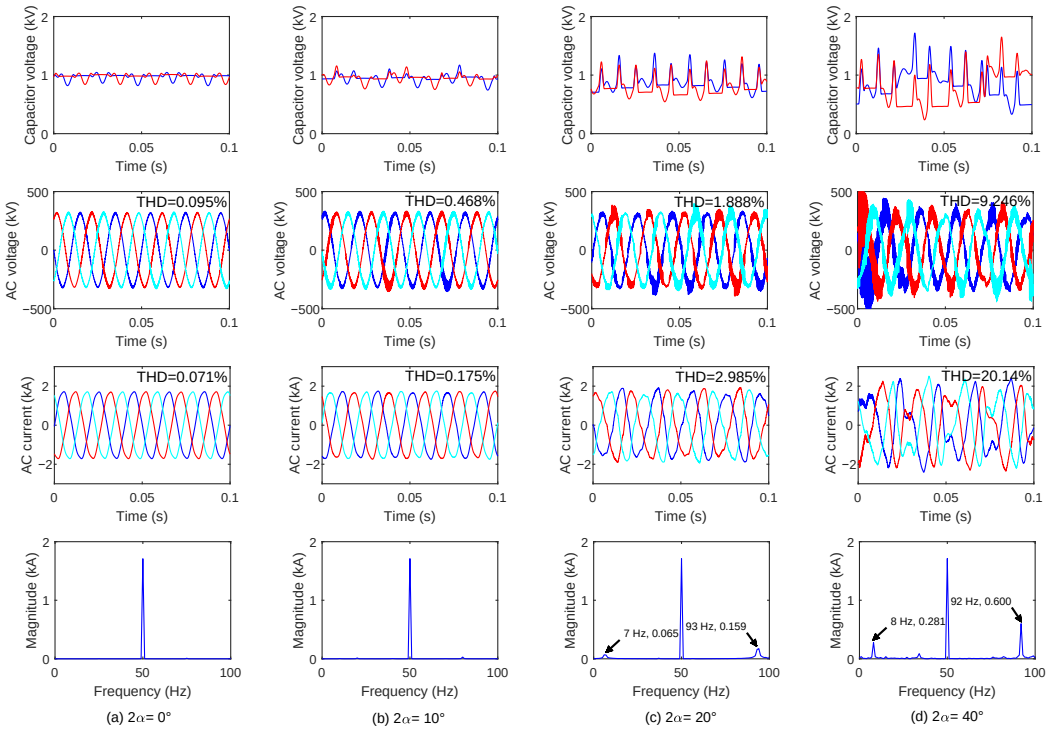

Figure 9. Simulation results of the AAC system with different overlap periods: (**a**) $2\alpha = 0°$; (**b**) $2\alpha = 10°$; (**c**) $2\alpha = 20°$; (**d**) $2\alpha = 40°$.

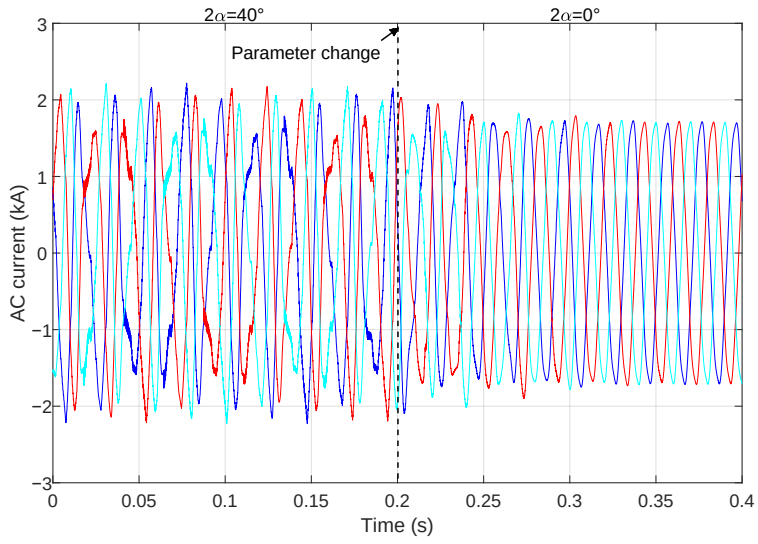

Figure 10. Waveform of AC current under parameter change.

The stability of AAC system with other SCRs can be evaluated in a similar way. The stability performance of AAC system deteriorates with weaker grid strength (i.e., smaller SCR) and the converter system will confront with resonance issues even with small overlap period. In contrast, when the SCR is larger than 17.6, the Eigenloci with different overlap periods are all located outside of the stability margin. This means that the AAC system with different overlap periods keeps stable when it is connected to a strong grid. To sum up, the Eigenloci that come from the impedance matrices give great insights into the evaluation of system stability and the identification of resonant frequencies.

6. Conclusions

In this paper, the impedance-based stability criterion in the *dq* frame is introduced to evaluate the stability of a grid-tied current controlled AAC system. The system stability can be reflected by the relationship between Eigenloci of return ratio matrix and the stability margin in Bode or polar plot. Eigenvalues that are located in the instability region might cause resonances at the corresponding resonant frequencies. Due to the *dq* decoupling control and the PLL effect, any identified resonant frequency in the *dq* frame will excite a pair of resonant frequencies in the AC current. The overlap period has its dominant impact on the stability of AAC at the low frequency range. The larger the overlap period is, the more unstable the AAC system becomes. The recommended set value for the fixed overlap period control or set range for the variable overlap period control in practical applications should not exceed 20°, especially in weak grids.

Author Contributions: Conceptualization, S.J. and G.K.; methodology, S.J.; software, S.J. and Z.S.; validation, S.J. and Z.S.; formal analysis, S.J.; investigation, S.J., F.A.-V. and G.K.; resources, G.K.; data curation, S.J. and G.K.; writing—original draft preparation, S.J. and F.A.-V.; writing—review and editing, S.J., F.A.-V., Z.S. and G.K.; visualization, S.J.; supervision, G.K.; project administration, G.K. All authors have read and agreed to the published version of the manuscript.

Funding: This research received no external funding.

Conflicts of Interest: The authors declare no conflict of interest.

Abbreviations

The following abbreviations are used in this manuscript:

AAC	Alternate Arm Converter
DS	Director Switch
PCC	Point of Common Coupling
SCR	Short-Circuit Ratio
GM	Gain Margin
PM	Phase Margin
PLL	Phase Locked Loop
SRF	Synchronous Reference Frame
THD	Total Harmonic Distortion
FFT	Fast Fourier Transformation

References

1. Debnath, S.; Qin, J.; Bahrani, B.; Saeedifard, M.; Barbosa, P. Operation, Control, and Applications of the Modular Multilevel Converter: A Review. *IEEE Trans. Power Electron.* **2015**, *30*, 37–53. [CrossRef]
2. Khazaei, J.; Beza, M.; Bongiorno, M. Impedance Analysis of Modular Multi-Level Converters Connected to Weak AC Grids. *IEEE Trans. Power Syst.* **2018**, *33*, 4015–4025. [CrossRef]
3. Sun, J. Impedance-Based Stability Criterion for Grid-Connected Inverters. *IEEE Trans. Power Electron.* **2011**, *26*, 3075–3078. [CrossRef]
4. Perez, M.A.; Ceballos, S.; Konstantinou, G.; Pou, J.; Aguilera, R.P. Modular Multilevel Converters: Recent Achievements and Challenges. *IEEE Open J. Ind. Electron. Soc.* **2021**, *2*, 224–239. [CrossRef]
5. Wang, X.; Blaabjerg, F. Harmonic Stability in Power Electronic-Based Power Systems: Concept, Modeling, and Analysis. *IEEE Trans. Smart Grid* **2019**, *10*, 2858–2870. [CrossRef]

6. Li, T.; Gole, A.M.; Zhao, C. Harmonic Instability in MMC-HVDC Converters Resulting From Internal Dynamics. *IEEE Trans. Power Deliv.* **2016**, *31*, 1738–1747. [CrossRef]
7. Gong, H.; Wang, X.; Yang, D. DQ-Frame Impedance Measurement of Three-Phase Converters Using Time-Domain MIMO Parametric Identification. *IEEE Trans. Power Electron.* **2021**, *36*, 2131–2142. [CrossRef]
8. Qi, Y.; Ar, G.; Hong, D.; Yi, Z. Evaluation of the Accuracy of Real-time Digital Simulator Voltage Source Converter Models Determined from Frequency Scanning. In Proceedings of the 2017 IPST Conference, Seoul, Korea, 26–29 June 2017; pp. 1–6.
9. Wen, B.; Burgos, R.; Boroyevich, D.; Mattavelli, P.; Shen, Z. AC Stability Analysis and dq Frame Impedance Specifications in Power-Electronics-Based Distributed Power Systems. *IEEE J. Emerg. Sel. Top. Power Electron.* **2017**, *5*, 1455–1465. [CrossRef]
10. Qi, Y.; Ding, H.; Zhang, Y.; Shi, X.; Gole, A.M. Identification of Sub-Synchronous Interaction in MMC Systems using Frequency Scanning. In Proceedings of the 2020 IEEE Power Energy Society General Meeting (PESGM), Montreal, QC, Canada, 2–6 August 2020; pp. 1–5. [CrossRef]
11. Wen, B.; Boroyevich, D.; Mattavelli, P.; Shen, Z.; Burgos, R. Influence of phase-locked loop on input admittance of three-phase voltage-source converters. In Proceedings of the 2013 Twenty-Eighth Annual IEEE Applied Power Electronics Conference and Exposition (APEC), Long Beach, CA, USA, 17–21 March 2013; pp. 897–904. [CrossRef]
12. Han, Y.; Yang, M.; Li, H.; Yang, P.; Xu, L.; Coelho, E.A.A.; Guerrero, J.M. Modeling and Stability Analysis of *LCL* -Type Grid-Connected Inverters: A Comprehensive Overview. *IEEE Access* **2019**, *7*, 114975–115001. [CrossRef]
13. Farr, E.M.; Feldman, R.; Clare, J.C.; Watson, A.J.; Wheeler, P.W. The Alternate Arm Converter (AAC)—"Short-Overlap" Mode Operation—Analysis and Design Parameter Selection. *IEEE Trans. Power Electron.* **2018**, *33*, 5641–5659. [CrossRef]
14. Wickramasinghe, H.R.; Konstantinou, G.; Pou, J. Gradient-Based Energy Balancing and Current Control for Alternate Arm Converters. *IEEE Trans. Power Deliv.* **2018**, *33*, 1459–1468. [CrossRef]
15. Liu, S.; Saeedifard, M.; Wang, X. Zero-Current Switching Control of the Alternate Arm HVdc Converter Station With an Extended Overlap Period. *IEEE Trans. Ind. Electron.* **2019**, *66*, 2355–2365. [CrossRef]
16. Wickramasinghe, H.R.; Sun, P.; Konstantinou, G. Interoperability of Modular Multilevel and Alternate Arm Converters in Hybrid HVDC Systems. *Energies* **2021**, *14*, 1363. [CrossRef]
17. Yang, H.; Fan, S.; Dong, Y.; Yang, H.; Li, W.; He, X. Arm Phase-Shift Conducting Modulation for Alternate Arm Multilevel Converter With Half-Bridge Submodules. *IEEE Trans. Power Electron.* **2021**, *36*, 5223–5235. [CrossRef]
18. Wickramasinghe, H.R.; Konstantinou, G.; Li, Z.; Pou, J. Alternate Arm Converters-Based HVDC Model Compatible With the CIGRE B4 DC Grid Test System. *IEEE Trans. Power Deliv.* **2019**, *34*, 149–159. [CrossRef]
19. Mohaddes, M.; Gole, A.; Elez, S. Steady state frequency response of STATCOM. *IEEE Trans. Power Deliv.* **2001**, *16*, 18–23. [CrossRef]
20. Merlin, M.M.C.; Green, T.C.; Mitcheson, P.D.; Trainer, D.R.; Critchley, R.; Crookes, W.; Hassan, F. The Alternate Arm Converter: A New Hybrid Multilevel Converter With DC-Fault Blocking Capability. *IEEE Trans. Power Deliv.* **2014**, *29*, 310–317. [CrossRef]
21. Gruson, F.; Vermeersch, P.; Guillaud, X.; Egrot, P. Energy control for the alternate arm converter. In Proceedings of the 2017 IEEE Manchester PowerTech, Manchester, UK, 18–22 June 2017; pp. 1–6. [CrossRef]